



## Probing single-cell mechanics with picosecond ultrasonics

Thomas Dehoux <sup>a,b</sup>, Maroun Abi Ghanem <sup>a,b</sup>, Omar F. Zouani <sup>c</sup>, Mathieu Ducousoo <sup>a,b</sup>, Nikolay Chigarev <sup>a,b,1</sup>, Clément Rossignol <sup>a,b</sup>, Nicolas Tsapis <sup>d</sup>, Marie-Christine Durrieu <sup>c</sup>, Bertrand Audoin <sup>a,b,\*</sup>

<sup>a</sup> Univ. Bordeaux, I2M, UMR 5295, F-33400 Talence, France

<sup>b</sup> CNRS, I2M, UMR 5295, F-33400 Talence, France

<sup>c</sup> Univ. Bordeaux, CBMN, UMR CNRS 5248, F-33607 Pessac, France

<sup>d</sup> Univ Paris-Sud, UMR CNRS 8612, Physicochimie-Pharmacotechnie-Biopharmacie, Faculté de Pharmacie, F-92296 Châtenay-Malabry, France

### ARTICLE INFO

#### Article history:

Received 6 February 2014

Received in revised form 10 July 2014

Accepted 15 July 2014

Available online xxxx

#### Keywords:

Picosecond ultrasonics

Cell mechanics

Cell adhesion

### ABSTRACT

The mechanical properties of cells play a key role in several fundamental biological processes, such as migration, proliferation, differentiation and tissue morphogenesis. The complexity of the inner cell composition and the intricate meshwork formed by transmembrane cell-substrate interactions demands a non-invasive technique to probe cell mechanics and cell adhesion at a subcell scale. In this paper we review the use of laser-generated GHz acoustic waves—a technique called picosecond ultrasonics (PU)—to probe the mechanical properties of single cells. We first describe applications to vegetal cells and biomimetic systems. We show how these systems can be used as simple models to understand more complex animal cells. We then present an opto-acoustic bio-transducer designed for *in vivo* measurements in physiological conditions. We illustrate the use of this transducer through the simultaneous probing of the density and compressibility of *Allium cepa* cells. Finally, we demonstrate that this technique can quantify animal-cell adhesion on metallic surfaces by analyzing the acoustic pulses reflected off the cell-metal interface. This innovative approach allows investigating quantitatively cell mechanics without fluorescent labels or mechanical contact to the cell.

© 2014 Elsevier B.V. All rights reserved.

## 1. Introduction

The ability of a biological cell to respond to mechanical cues sent by the extracellular microenvironment plays a key role in several fundamental biological processes, such as migration, proliferation, differentiation and tissue morphogenesis [1–4]. However, the precise mechanisms that underlie these responses remain largely undetermined, partly due to the lack of a clear description of the mechanical properties of the cell, notably of the nucleus and of the cytoskeleton.

The cell nucleus directs all cell activity and regulates gene expression [1]. Nuclear mechanics and structural integrity have been shown to be critical for a variety of cellular functions and when altered, for example, by mutations of the lamina proteins, may contribute to different diseases such as muscular dystrophy [5,6]. It has also been postulated that the access of specific transcription factors to their binding sites and gene expression can

be modulated by nuclear deformations [7]. Finally it is well established that forces can be transmitted through the cytoskeleton toward the nucleus because there is a constant physical interplay between these two structures [1,8]. This illustrates that nuclear activity is closely related to its mechanical properties.

During interaction with its microenvironment, the cell forms microscale adhesions that serve as anchors for the structuration of the cytoskeletal network within the cytoplasm. External forces exerted on the cell transit through this structure and allow the cell to sense its surrounding environment. This process called mechanosensation is key to fundamental cellular processes involving motility or changes in cell shape, such as migration, proliferation or morphogenesis [1,3,9]. Probing the mechanics of this highly heterogeneous cell-substrate interface is therefore of utmost importance in determining the mechanisms of cell adhesion, and requires subcell characterization.

Fluorescence-based techniques allow imaging the separation distance of labeled membrane-proteins from biomaterial surfaces [10,11]. Interference reflection microscopy provides precise localization of focal adhesion sites [12]. Recent surface plasmon resonance microscopy has allowed label-free imaging of the refractive index changes in the vicinity of adhesion zones [13].

\* Corresponding author at: Univ. Bordeaux, I2M, UMR 5295, F-33400 Talence, France.

E-mail address: bertrand.audoin@u-bordeaux1.fr (B. Audoin).

<sup>1</sup> Present address: LAUM, UMR-CNRS 6613, Université du Maine, 72085 Le Mans, France.

To obtain quantitative measurement of the adhesion force, single-cell force microscopy requires direct contact to the cell [14–16] or the use of nanostructured substrates as an array of mechanical contact-probes [17–19]. However, none of these techniques can quantify adhesion strength at a subcell scale in a non-contact manner.

Regarding the measurement of the mechanical properties of cells at a subcell scale, the vast majority of these techniques are probe-based and the measured mechanical properties are highly dependent on the linkages between the probe and the cell. This may lead to significant under- or over-estimation of the overall stiffness [20]. Moreover, as opposed to active techniques, which induce cellular motion in a controlled manner, passive techniques rely on the spontaneous diffusive motion of Brownian probes. In this case, non-Brownian motions induced by active intracellular processes may confound the sole contribution of the mechanical properties of the cell. For this, passive microrheology is best suited to cells in which biological activity is chemically inhibited, such ATP-depleted cells [21]. Clearly, there is need for a non-invasive technique that would allow probing cell mechanics during biological processes, as well as cell adhesion, at a subcell scale.

We report on the use of laser-generated GHz acoustic waves—a technique called picosecond ultrasonics (PU)—to probe the mechanical properties of vegetal cells [22–25], animal cells [26,27], as well as cell-mimicking micro-objects [28]. This non-contact technique developed in the mid-80's was traditionally devoted to the investigation of solids [29,30]. PU has permitted mapping of the mechanical, thermal and optical properties of metals [31], semi-conductors [32] and amorphous materials [33]. It offers a broad frequency range extending up to 1 THz, a sub-micrometer lateral resolution and nanometer in-depth resolution [34,29,30]. Such resolution is very well suited to cell imaging at a subcell scale, and for this reason it was soon foreseen that PU would be a powerful tool to investigate the mechanics of single cells.

Regarding liquid systems, PU was used to measure reflections from solid–liquid interfaces [35]. The measurement of the acoustic reflection coefficient from a Al/water interface has also been used to design an acoustic microscope with nanometer resolution [36]. The propagation of bulk GHz acoustic waves has allowed the mechanical characterization of Langmuir–Blodgett films [37] and colloids [38,39]. Later measurements of the longitudinal sound velocity in water [40], of shear relaxation in thin glycerol films [41] or of phonon dispersion in liquid mercury [42] have demonstrated the ability of PU to probe non-absorbing liquids. Specific setups have been designed to probe acoustic propagation in strongly scattering liquids [43]. Despite these innovative developments, the use of PU to investigate soft matter remains elusive and extremely challenging, and applications to cells are lacking.

In this paper, we review applications of PU to single cells. We first investigate the mechanical properties of vegetal cells and of biomimetic systems. We show how these systems can be used as simple models to understand more complex animal cells. We then present an opto-acoustic bio-transducer designed for *in vivo* measurement in physiological conditions. We apply this transducer to the simultaneous probing of the density and compressibility of onion cells. In the last section, we probe animal-cell adhesion on metallic surfaces by taking advantage of the dispersion of the acoustic reflection coefficient.

## 2. Defining model systems

Animal cells have a complex structure composed mainly of the cytoskeleton and of the nucleus. The cytoskeleton is an arrangement of actin fibers that assemble and disassemble to allow

various biological transitions, such as migration, differentiation or morphogenesis [44]. The nucleus contains mostly the cell DNA, wrapped around histones to form longer fibrous elements that assemble into a larger scale scaffold. This structure of the cell yields an intricate mechanical behavior that is highly frequency dependent and resembles that of a polymer blend [45]. To demonstrate the applicability of PU to single-cell biology, we consider in this section simpler systems. We first show results on vegetal cells, which lack cytoskeleton. We then consider polymer bio-mimetic micro-objects to simulate the glassy behavior of cells in the GHz range.

### 2.1. Vegetal cells

Common onion samples (*Allium cepa L.*) were acquired commercially for all experiments. The second scale of fresh and healthy onion bulbs were selected to avoid either not fully-hydrated cells from the outermost layer or non-mature cells from the inner bulb core. The epidermis was cut longitudinally, parallel to the vascular bundles, into rectangular pieces with a clean surgical knife. These epidermal strips with approximate dimensions  $2 \times 6$  mm were carefully removed from the equatorial region of the inner tissue surface. A top-view white-light image of the cells is shown in Fig. 1(a). We placed the strip on a Ti6Al4V half-space for photoelastic transduction, and pressed gently (see Fig. 1(b) and Ref. [22]).

We used an optical pump–probe technique described schematically in Fig. 2. Optical pulses of duration 100 fs, repetition frequency  $f_r = 80$  MHz, wavelength  $\lambda_{pp} = 790$  nm were generated by a Ti:Sapphire mode-locked laser. Frequency-doubled pump pulse trains of wavelength 395 nm were chopped at a frequency  $f_m = 330$  kHz for lock-in detection. The 790 nm probe beam passed through a mechanical delay line to tune the pump–probe time delay  $t$ . The reflected probe beam was sent to a photodiode to measure the change in optical reflectivity  $\delta R$  as a function of  $t$ . For the experiments presented in this section, both pump and probe beams were focused on the top side of the bulk Ti6Al4V half-space using a  $\times 50$  objective lens [see Fig. 1(b)]. This part of the setup is indicated with a gray square in Fig. 2. Each pump pulse is initially absorbed in the metal layer over a depth comparable to the optical skin depth  $1/\beta_1 \sim 15$  nm [23]. Conduction band electrons are excited and diffuse over a depth of  $(\kappa_1/g_1)^{1/2} = 2$  nm during their thermalization with the lattice, where  $\kappa_1 = 3.1 \text{ W m}^{-1} \text{ K}^{-1}$  and  $g_1 = 13 \times 10^{17} \text{ W m}^{-3} \text{ K}^{-1}$  are the thermal conductivity [23] and electron–phonon coupling constant in Ti [46], respectively. The

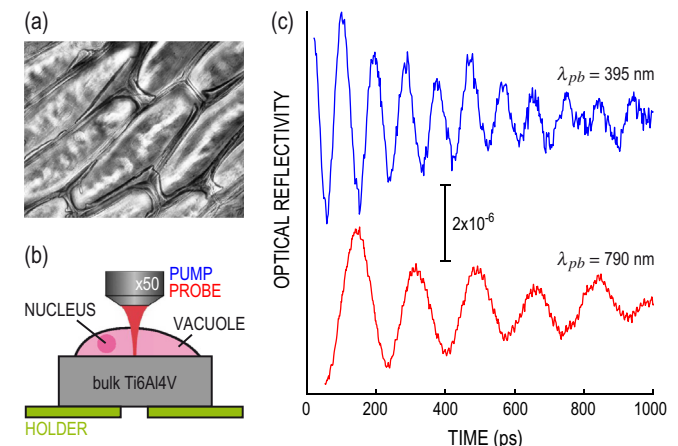


**Fig. 1.** (a) Top view of typical onion cells. (b) Bulk Ti6Al4V alloy-based transducer. (c) Optical reflectivity measured with an ultrafast laser probe of wavelength  $\lambda = 395$  nm (top curve) and  $\lambda = 790$  nm (bottom curve) in the vacuole of a single onion cell.

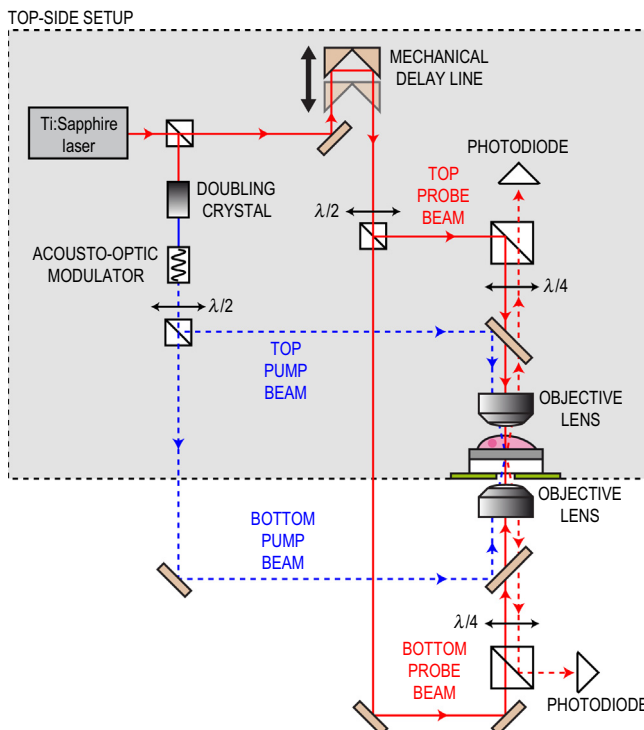


**Fig. 2.** Simplified scheme of the set-up. The pump and probe beams can be alternatively focused on the top or on the bottom surface of the Ti film. The setup where the coaxial pump and probe beams are focused through the cell (or capsule) at the top surface of the transducer is indicated by the gray square.

subsequent thermoelastic expansion generates in Ti a longitudinal acoustic pulse with a duration of a few picoseconds. The absorbed heat diffuses in the lattice on a larger nanosecond timescale.

The excitation of overheated electrons causes a sharp rise in  $\delta R$  used to define time  $t = 0$ . This rise is followed by a slower decrease owing to heat diffusion. To observe only the contribution of acoustic waves to the optical reflectivity, we removed the contributions of overheated electrons and thermal diffusion by subtracting a polynomial. The resulting  $\delta R$  is plotted in Fig. 1(c) (bottom curve). The ultrafast thermal dilatation of the metal launches a compressional sound pulse. Due to Ti6Al4V-cell contact, a compressional sound pulse is simultaneously transmitted to the cell, and propagates in the vacuole. This pulse induces infinitesimal strain with an amplitude of  $\sim 10^{-6}$ . The probe beam is partially reflected from the Ti surface and partially scattered by the acoustic wavefront propagating in the cell. Interferences arise from these two probe contributions and cause the so-called Brillouin oscillations [30]. The frequency of the oscillations is

$$f_b = \frac{2n_v v_v}{\lambda_{pb}} \quad (1)$$

where  $\lambda_{pb} = 790$  nm,  $n_v = 1.35$  [47] and  $v_v$  are the probe wavelength, the refractive index and the sound velocity of the cell vacuole, respectively. A Fourier transform gave  $f_b = 5.5 \pm 0.1$  GHz, and allowed measuring the sound velocity in the cell,  $v_v = 1660 \pm 30$  m/s [23].<sup>2</sup> These values were obtained as a result of measurements at ten different locations inside the same vacuole [22]. As a comparison, the sound velocity in pure water at 22 °C is 1490 m/s [48]. The sound velocity in the vacuole is thus close to that of water,

<sup>2</sup> We estimated the error on Brillouin frequency to be 0.1 GHz, that is 1/10th of the acquisition time window. The subsequent errors on the velocity were estimated by differentiating Eq. (1).

as expected since the vacuole is filled only by liquids. Similarly, we found a velocity of  $v_n = 2000 \pm 30$  m/s in the nucleus (averaged over 10 cells) [23].

To confirm that these oscillations arised from a photoelastic interaction in the cell, we switched the pump and probe wavelengths to perform the same experiment using  $\lambda_{pb} = 395$  nm in the same cell. The measured  $\delta R$  is plotted in Fig. 1(c) (top curve). We found a frequency  $f_b = 11 \pm 0.1$  GHz which is exactly twice that measured with a probe wavelength  $\lambda_{pb} = 790$  nm. This comparison demonstrates that we were indeed measuring Brillouin oscillations in the cell, and indicates that the refractive index does not vary for this range of optical wavelength. This observation suggests this technique could be used to study the optical properties of the cell. Once the sound velocity is determined, one could indeed investigate the influence of external stimuli, such as pH or calcium concentration on the refractive index. This is particularly important in studying, for instance, the transmittivity of leaves [49,50].

To evaluate the invasiveness of the technique, we calculated the total stress at a typical cell-metal interface. Temperature rise  $T$  following laser absorption in the metal layer is described by the Fourier equation. We solved the one-dimensional elastic wave equation for a source term proportional to  $\nabla T$ . We found a maximum acoustic stress of about 200 Pa that lasts for a few picoseconds [23]. As a comparison, adhesion forces measured for osteoblast cells on glass are about 1  $\mu$ N, corresponding to adhesion stresses of several kPa [51]. The acoustic stress generated with the picosecond ultrasonics technique is thus much lower than this adhesion stress, making the technique completely non-invasive.

It is also important to verify that the laser power is low enough to maintain physiological conditions. On the normative point of view, the maximum electromagnetic radiation to which human tissues can be exposed has been estimated as a function of the electromagnetic wavelength, exposure time, and pulse repetition. The International Electrotechnical Commission [52] and the American National Standard [53] defined a maximum permissible exposure (MPE) level of 20 mJ/cm<sup>2</sup> for a 400 nm wavelength and a pulse duration of 1–100 ns. Several biomedical applications in which femtosecond lasers are focused in a cell have already been developed. Femtosecond laser pulses have been used for two-photon optical imaging of tissues without observing morphological changes of the cell [54–56]. At a cell scale, it has been shown that vitality and proliferation of cells remain unaffected by light pulses similar to those used in this paper in terms of focusing, pulse duration, wavelength and repetition rate for mean power up to 1 mW [57]. This threshold is comparable to the mean laser power we use here [23].

These results are the first reported in literature about the use of PU to probe cells. They demonstrate the ability of PU for the non-invasive probing of the mechanical properties (sound velocity and attenuation) of the organelles of single live cells. Such experiments have also established onion cells as a simple, widely available and well documented biological model to develop the application of PU to single cell biology. However, animal cells have a much more complex composition, mostly due to the presence of actin filaments which are not found in vegetal cells. The sophisticated structure of animal cells yields an intricate mechanical behavior resembling that found in polymer networks [58]. To mimic this behavior, we therefore developed a confined polymer system based on microcapsules [28].

## 2.2. Microcapsules as model soft-glass system

Stress relaxation in cells arises from unbinding events and conformational changes. The heterogeneity of the internal cell structure yields multiple closely spaced relaxation times [21]. This metastable nature of the cytoplasm has been recently compared

to that of soft glasses [59]. To mimick this behavior, we designed a soft glassy polymer micro-object.

Soft polymer micro-objects are indeed of great interest for their encapsulation capacities [60–62], their use as contrast agents for ultrasonic imaging [63–65], as well as their cell-mimicking properties [66]. Their compressibility, viscosity and membrane thickness play an important role in the way they react to external stimuli such as pH change [67] or mechanical stress [68]. Similarly to cells, the relaxation mechanisms of polymer micro-objects, like such of multiple-phase core-shell capsules, are expected to differ greatly from that of the bulk materials they are made of, because of polymer shell dynamic confinement, and of core–shell interfacial interactions, as observed for thin polymer films [69,70]. For these reasons, microcapsules are a perfect model system to mimick in a controlled manner the behavior of cells. In this section, we use PU to probe in a liquid environment the viscoelastic properties and shell thickness of single spherical microcapsules, composed of a glassy polymer shell encapsulating a liquid perfluorinated core.

We prepared microcapsules composed of a biodegradable poly(lactide-co-glycolide) shell (PLGA, 50:50, Resomer RG502, Boehringer-Ingelheim, MW 12 kDa) encapsulating a liquid perfluorooctyl bromide core (PFOB, C<sub>8</sub>F<sub>17</sub>Br) by a classical solvent emulsion-evaporation technique. Such microcapsules have been successfully evaluated as ultrasound contrast agents [63]. PLGA was dissolved in methylene chloride along with PFOB. The quantity of dissolved PLGA was adjusted to modulate the shell thickness from ~1 μm down to ~100 nm. The organic solution was then emulsified into a surfactant aqueous solution before being evaporated. Fig. 3(a) and (b) shows scanning electron microscopy (SEM) and confocal fluorescent microscopy images of capsules of thickness-to-radius ratio ~0.25, respectively. The capsules were freeze-dried for long-term storage, and hydrated on demand with deionized water one hour prior to the laser investigation. A drop of the water solution containing the capsules was placed on a Ti6Al4V half-space. The sample was covered with a transparent glass window to prevent evaporation. To limit Brownian motion and transport by laser heat-induced convection, we investigated capsules of radius estimated optically at  $R \approx 4 \mu\text{m}$ . The room temperature was maintained at ~23 °C during the whole experiment, below the glass transition of PLGA (39 °C measured by differential scanning calorimetry).

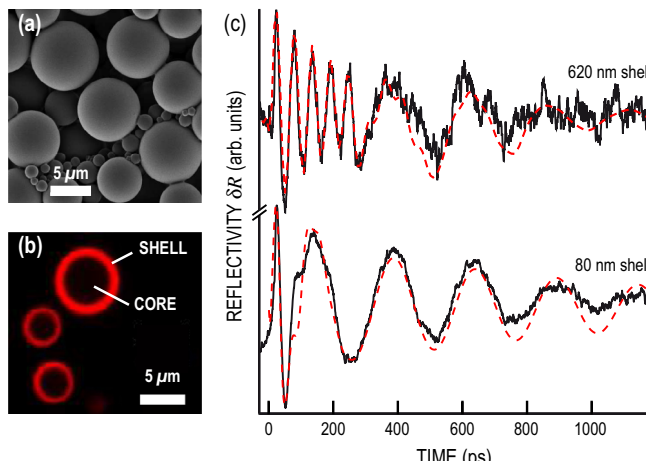


**Fig. 3.** (a) SEM images. (b) Confocal microscopy with PLGA dyed in red. (c) Optical reflectivity  $\Delta R$  measured (plain black lines) and calculated (red dotted lines) for capsules of shell thickness 620 and 80 nm. (For interpretation of the references to color in this figure legend, the reader is referred to the web version of this article.)

The low-energy coaxial pump (800 nm) and frequency-doubled probe ( $\lambda_{pb} = 400 \text{ nm}$ ) beams were focused through the top of the capsule at the Ti6Al4V-capsule interface as explained previously (top-side setup in Fig. 2). Fig. 3(c) (top curve) shows  $\Delta R(t)$  measured in a thick-shell capsule. A polynomial was subtracted to remove the contribution of incoherent phonons diffusing in Ti6Al4V. The photoelastic interaction of the probe light of wavelength  $\lambda_{pb}$  with the acoustic pulse propagating in the transparent capsule produces Brillouin oscillations at a frequency  $f_m = 2n_m v_m / \lambda_{pb}$ , where  $n_m$  and  $v_m$  are the refractive index and the longitudinal sound velocity, respectively (index  $m = s, c$  stands for the shell and the core). A short-time Fourier transform indicates that a first frequency  $f_s = 18 \pm 0.3 \text{ GHz}$  arises within the first ~250 ps, followed by a second frequency  $f_c = 4 \pm 0.1 \text{ GHz}$ , revealing the successive contributions of the shell and of the core. The bottom curve in Fig. 3(c) shows similar data measured in a much thinner-shell capsule. The transition time between  $f_s$  and  $f_c$  allows determination of the shell thicknesses at 620 and 80 nm [28]. These thicknesses are in excellent agreement with those estimated from confocal microscopy images. Using the refractive indices  $n_s = 1.5$  (measured by index matching) and  $n_c = 1.3$  [71],  $f_s$  and  $f_c$  yield  $v_s = 2400 \pm 40 \text{ m s}^{-1}$  and  $v_c = 610 \pm 20 \text{ m s}^{-1}$ . These values match closely the velocities found in the literature at 10 MHz [72,73].

The lifetime of the Brillouin oscillations, related to the relaxation processes, yields the attenuation in the shell at  $\Gamma_s = 1.8 \pm 0.1 \mu\text{m}^{-1}$  for both capsules.<sup>3</sup> Since the phonon wavelength  $\lambda_{pb}/2n_s \ll \Gamma_s^{-1}$ , the longitudinal storage and loss moduli of the shell are defined as  $M'_s = \rho_s v_s^2 = 8 \pm 0.1 \text{ GPa}$  and  $M''_s = 2v_s^3 \Gamma_s \rho_s / 2\pi f_s = 0.6 \pm 0.04 \text{ GPa}$ , respectively, where  $\rho_s = 1.35 \text{ g/cm}^3$  is the mass density [74]. The longitudinal kinematic viscosity, defined as  $\eta_L^s = M''_s / 2\pi f_s \rho_s = 4 \pm 0.7 \text{ mm}^2/\text{s}$ , lies within the range observed in glassy polymers at GHz frequencies [75]. We now compare our data with lower frequency bulk PLGA values. From the longitudinal sound velocity and attenuation measured by Parker et al. [73] at 10 MHz, we calculate similarly  $M'_s \approx 8 \text{ GPa}$  and  $M''_s \approx 0.1 \text{ GPa}$ . This weak  $f_s$ -dependence of  $M''_s$  is the signature of thermally activated processes in glasses. We simultaneously determine the attenuation in the PFOB core at  $\Gamma_c = 1.6 \pm 0.1 \mu\text{m}^{-1}$ , giving a longitudinal kinematic viscosity  $\eta_L^c = 1.2 \pm 0.2 \text{ mm}^2/\text{s}$  associated with the Kelvin-Voigt analogy. This value is in agreement with that given in the literature at 10 MHz and 25 °C [71], demonstrating that the frequency dispersion is negligible for such a low viscosity liquid.

These results demonstrate the ability of PU to probe GHz-phonon relaxation in each compartment of a confined multiple-phase microobject. Structures as small as 80 nm have been identified. In this frequency range, the frequency-dependence of the complex elastic modulus is driven by thermally-activated processes, which is of utmost importance to describe viscous dissipation in animal cells. In view of obtaining more information on the mechanical properties of cells, we developed an opto-acoustic bio-transducer, as detailed in the following.

### 3. An opto-acoustic bio-transducer for single-cell probing

In the experiments presented in the previous section, biological samples were placed onto a biometallic half-space to generate acoustic waves through the absorption of laser pulses at the sample-metal interface [22,23]. This configuration has allowed the direct determination of the sound velocity and attenuation in single cells at GHz frequencies through the Brillouin acousto-optic

<sup>3</sup> To estimate the error on the attenuations, we consider that the minimum detectable exponential decrease in the amplitude of the Brillouin oscillation during the observation time window  $T$ ,  $\exp(-\Gamma_m v_m T)$ , is 95% of the maximum amplitude. In other words, we consider an error of  $\ln(0.95)/v_m T$  on the attenuation  $\Gamma_m$ .

interaction [22,23], opening pristine fields for the investigation of physiological processes at a sub-cell scale. The first limitation of this configuration is that the temperature rise is maximal at the cell–metal interface, thus imposing to reduce the fluence of the laser to maintain physiological conditions. The second limitation is that the roughness, the curvature of the cell surfaces and the optical propagation through several biological layers may distort the laser beams, and restrict the inspected area.

In this section, we present an opto-acoustic bio-transducer designed for *in vitro* measurements in physiological conditions. It is composed of a thin metal film sputtered on a transparent heat sink. In order to optimize the design of the transducer, we first model semi-analytically thermal diffusion within the transducer to describe heat dissipation [24]. We then use the opto-acoustic bio-transducer to characterize simultaneously the density and compressibility of single cells by measuring acoustic reflections at the cell–transducer interface and Brillouin interaction in the cell [76,24]. We finally show how the opto-acoustic bio-transducer can be used to map the adhesion of single cells by taking advantage of the frequency-dependence of the reflection coefficient [26].

### 3.1. Thermal design of the transducer

Titanium-based alloys are commonly used as structural biomaterials for the replacement of hard tissues in artificial joints and they display the most suitable biomedical properties. To reproduce this metallic interface, we deposited a thin (300–500 nm) polycrystalline titanium film on a transparent substrate. Single cells were placed on the top surface of the metal film. The geometry of this opto-acoustic transducer is shown in Fig. 4. Since the substrate is transparent, it allows focusing the pump laser beam at the Ti–SiO<sub>2</sub> interface without damage to the material placed onto the top Ti surface [77]. To quantify the non-invasive nature of such a transducer, we estimate the temperature rise at the surface of the transducer upon laser absorption.

The pump light is absorbed in Ti over a nanometer depth comparable with the optical skin depth. The subsequent thermoelastic expansion generates in Ti a longitudinal acoustic pulse with a duration of a few picoseconds. The absorbed heat diffuses on a larger nanosecond timescale. To describe heat transport, we solved the diffusion equation for a Fourier flux. Owing to the axial symmetry of the pump beam, we used the cylindrical coordinates (*r*, *z*), where *r* and *z* are the radial and axial coordinates. The Ti film and the transparent substrate are called medium 1 and medium 2, respectively (see Fig. 4). In order to evaluate the temperature as a function of the modulation frequency in medium *i* = 1, 2, we considered an harmonic temperature field  $T_i(r, z, t) = \theta_i(r, z, \omega) \exp(j\omega t)$  of angular frequency  $\omega$ , where  $\theta_i$  is a solution of [78]:

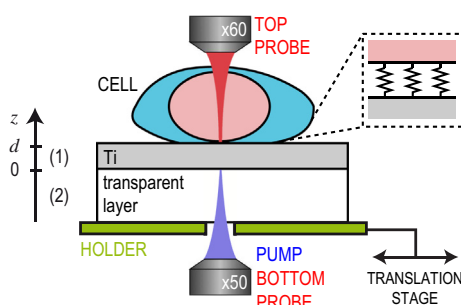


**Fig. 4.** Transducer geometry. The pump is focused on the bottom side of the Ti film. The probe beam can be alternatively focused on the top or on the bottom surface of the Ti film. The sample is placed on a high-precision translation stage to map the Ti–cell interface.

$$\Delta\theta_i(r, z, \omega) - \frac{j}{\alpha_i^2} \theta_i(r, z, \omega) = \delta_{1i} S(z) e^{-2r^2/\chi^2} \quad (2)$$

The Kronecker delta  $\delta_{1i}$  indicates that the source term is only appearing in medium 1 owing to optical absorption in Ti. Since the pump was focused at the substrate-Ti interface,  $S(z) = S_0 \exp(-\beta_1 z)$ , where  $S_0$  is the absorbed intensity and  $1/\beta_1$  is the optical skin depth in Ti. The variable  $\alpha_i = (\kappa_i/\rho_i C_{pi})^{1/2}$  is the thermal diffusion length, with  $\kappa_i$ ,  $\rho_i$  and  $C_{pi}$  the thermal conductivity, mass density and specific heat, respectively. The variable  $\chi$  is the effective radius at  $1/e^2$  of the lateral Gauss distribution of the beam intensity, calculated as  $\chi = (\chi_{pp}^2 + \chi_{pb}^2)^{1/2}$ .

Owing to the axial symmetry, we decomposed the solution  $\theta_i(r, z, \omega)$  on zero-order Bessel functions of the first kind  $J_0$  using a zero-order Hankel transform:

$$\Omega_i(k, z, \omega) = \int_0^\infty \theta_i(r, z, \omega) J_0(kr) r dr \quad (3)$$

where *k* is the wavenumber. Eq. (2) becomes:

$$\frac{\partial^2 \Omega_i}{\partial z^2} - \eta_i^2 \Omega_i = \delta_{1i} G(k) S(z) \quad (4)$$

with  $G(k) = -(\chi^2/4) \exp(-k^2 \chi^2/8)$  and  $\eta_i^2 = k^2 + j/\alpha_i^2$ . We neglect the thermal boundary resistance and assume continuity of the temperature and of the heat flux at the Ti–substrate interface. In this configuration, the temperature at the top surface of the transducer (*z* = *d*, where *d* is the film thickness) is:

$$\Omega_t(k, \omega) = \frac{g_2 S_0}{\eta_1^2 - \beta_1^2} \left[ \frac{2 \left( Z - \frac{\beta_1}{\eta_1} \right) e^{-\eta_1 d}}{(Z+1) + (Z-1)e^{-2\eta_1 d}} + e^{-\beta_1 d} \right] \quad (5)$$

where  $Z = \kappa_2 \eta_2 / \kappa_1 \eta_1$  is the ratio of the thermal impedances. The reduction of the transmitted pump intensity owing to the presence of the substrate is taken into account in the expression of  $S_0$  by introducing the optical reflection coefficient at the uncoated bottom surface of the transparent substrate. In Ti,  $1/\beta_1 \sim 15$  nm, and  $\beta_1 d \gg 1$ . Therefore neither the pump radiation nor the overheated electrons reach the top Ti surface where the cell is deposited in the case where the pump is focused on the bottom side of the Ti film. This would be also valid for any metal with a high electron-phonon coupling constant.

We plot the inverse Hankel transform of  $\Omega_t$  evaluated at the center of the pump beam (*r* = 0) vs frequency in Fig. 5 for a Ti film of thickness 500 nm, deposited on SiO<sub>2</sub> or on Al<sub>2</sub>O<sub>3</sub> with a blue or red line, respectively. The thermal properties of the media we evaluated are summarized in Table 1. The effective radius was adjusted to  $\chi = 2.1$  μm to match the experimental conditions used in the next sections. The  $\omega$ -dependence arises from  $\eta_i$  which contain the diffusion length  $\alpha_i$  (see Eq. (5)). For comparison, we plot with a black line the temperature calculated at the surface of a bulk half-space. We observe that for typical modulation frequencies  $f_m = 0.1$ –10 MHz, the use of a Ti film rather than a bulk half space allows reducing the temperature at the surface of the transducer by a factor 2 in the case of SiO<sub>2</sub>, and by a factor 14 in the case of Al<sub>2</sub>O<sub>3</sub>. This analysis confirms that using a transparent substrate with a high thermal conductivity  $\kappa_2$  (such as Al<sub>2</sub>O<sub>3</sub>) is the most favorable configuration. In this case the heat diffuses predominantly in the substrate and the temperature rise at the surface of the transducer is therefore greatly reduced.

For comparison, the temperature at the bottom of the Ti film, at the interface with the transparent substrate (*z* = 0) is:

$$\Omega_b(k, \omega) = \frac{g_2 S_0}{\eta_1^2 - \beta_1^2} \left[ \frac{\left( Z - \frac{\beta_1}{\eta_1} \right) (1 + e^{-2\eta_1 d})}{(Z+1) + (Z-1)e^{-2\eta_1 d}} + 1 \right] \quad (6)$$

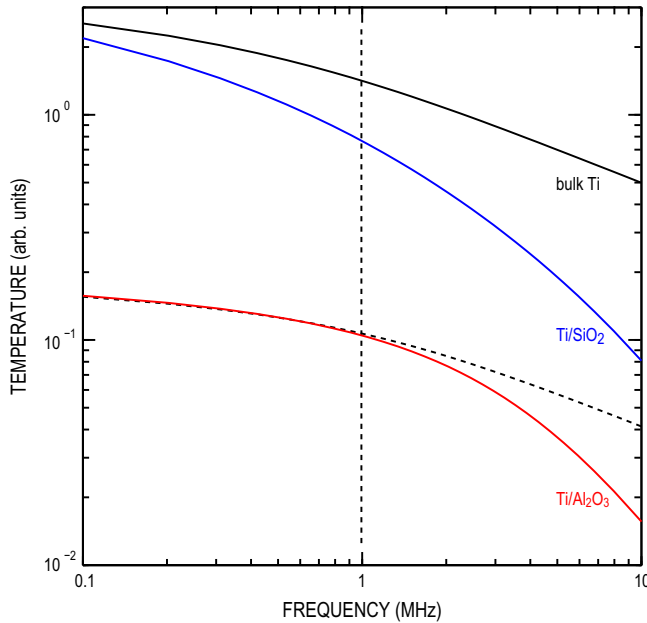


**Fig. 5.** Temperature rise at the center of the pump beam at the surface of a bulk Ti half-space (black), of a Ti-SiO<sub>2</sub> transducer (blue) and of a Ti-Al<sub>2</sub>O<sub>3</sub> transducer (red). The temperature rise at the Ti-Al<sub>2</sub>O<sub>3</sub> interface is plotted with a dotted line. (For interpretation of the references to color in this figure legend, the reader is referred to the web version of this article.)

**Table 1**

Thermal properties of the Ti, SiO<sub>2</sub> and Al<sub>2</sub>O<sub>3</sub> [23,77]. The thermal conductivity of the Ti film is assumed to be 1/7 of the single-crystal value [77].

|   | Ti   | SiO <sub>2</sub> | Al <sub>2</sub> O <sub>3</sub> |
|---|------|------------------|--------------------------------|
| $\rho_t$ (kg m <sup>-3</sup> )                  | 4500 | 2200             | 4000                           |
| $C_{pi}$ (J kg <sup>-1</sup> K <sup>-1</sup> )  | 500  | 745              | 850                            |
| $\kappa_t$ (W m <sup>-1</sup> K <sup>-1</sup> ) | 3.1  | 1.4              | 45                             |

As expected,  $\Omega_t \rightarrow \Omega_b$  when  $d \rightarrow 0$ . We plot with a dotted line  $\Omega_b$  vs frequency in Fig. 5 for a Ti film of thickness 500 nm deposited on Al<sub>2</sub>O<sub>3</sub> (see Table 1). At frequencies below a critical frequency  $f_c \approx 1$ , indicated by the vertical dotted line, the diffusion length in Ti is greater than the film thickness,  $\eta_1 d \ll 1$ . In this case  $\Omega_b = \Omega_t$ , meaning that thermal confinement occurs in the Ti layer. Beyond  $f_c$ ,  $\Omega_t \ll \Omega_b$  and the temperature rise at the Ti-substrate interface does not reach the top Ti surface where the cells are deposited. In the remainder, we therefore choose  $f_m = 1$  MHz to limit thermal confinement while keeping a good signal-to-noise ratio. The analytical modeling has thus allowed us to optimize the design of the transducer (thickness, substrate diffusivity and modulation frequency) to reduce temperature rise at the cell-transducer interface.

### 3.2. Simultaneous probing of the density and compressibility of an *Allium cepa* cell

We now use the opto-acoustic bio-transducer described above to measure simultaneously the acoustic reflection coefficient and the Brillouin oscillations. We applied this procedure to determine both the density and compressibility of a single *Allium cepa* cell. Since such cells withstand higher fluences than animal cells do, we used a SiO<sub>2</sub> substrate as a cheap alternative to Al<sub>2</sub>O<sub>3</sub>. We deposited a 500 nm thick polycrystalline titanium film on a SiO<sub>2</sub> substrate by RF sputtering. The pump was focused at the bottom of the Ti film to reduce thermal stress to the cell, and the probe beam was focused on the top surface of the transducer, through the cell

(see Fig. 2). To characterize the bandwidth of the transducer, we plot in Fig. 6(a) the reflectivity change  $\delta R$  measured on the bare transducer. No transient-temperature rise is observed, indicating that the thermal diffusion length at the laser repetition frequency  $f_r$  is smaller than the Ti film thickness. Due to the relatively low acoustic mismatch at the Ti-SiO<sub>2</sub> interface (acoustic reflection coefficient  $R_{ts} = 0.22$ ), the thermoelastic generation at the Ti-SiO<sub>2</sub> interface launches almost unipolar strain pulses in the Ti film and in the SiO<sub>2</sub> substrate [77]. The unipolar pulse propagating in Ti is detected as a bipolar echo, at times 140 and 290 ps due to the successive reflections at the film interfaces. The amplitude of the Fourier spectrum of the echoes plotted in the inset of Fig. 6(a) reveals a broad frequency bandwidth centered around 50 GHz, and extending up to  $\sim 120$  GHz.

We extracted the amplitudes of the echoes using a wavelet analysis at a given frequency. We used a Morlet wavelet defined by

$$W_m(t) = \cos(4\alpha t) \exp[-(\alpha t)^2/2] \quad (7)$$

where the scaling factor  $\alpha$  controls the center frequency of the wavelet  $f_w$ . For more accurate results, we chose a 50 GHz wavelet located at the center of the acoustic bandwidth [see dotted line in the inset of Fig. 6(a)]. The convolution of the transient  $\delta R$  measured on the bare transducer with the wavelet is plotted in Fig. 7 with a plain line. The first two echoes are clearly visible. The ratio of the second to the first echo yields the acoustic reflection coefficient  $R_{ts} = (Z_t - Z_s)/(Z_t + Z_s) = 0.22$  at the Ti-SiO<sub>2</sub> interface, where  $Z_t$  and  $Z_s$  are the acoustic impedances of Ti and SiO<sub>2</sub>, respectively. The longitudinal sound velocity in SiO<sub>2</sub>  $v_s = 5790$  m s<sup>-1</sup> was determined from the Brillouin frequency (measured separately [24], not shown), and from the refractive index  $n_s = 1.45$ . The acoustic impedance of SiO<sub>2</sub> is therefore  $Z_s = \rho_s v_s = 12.7$  MPa s m<sup>-1</sup>, where  $\rho_s = 2.2$  g cm<sup>-3</sup> is the mass density. Based on this value, the impedance of the Ti film  $Z_t = 19.5$  MPa s m<sup>-1</sup> can be deduced from  $R_{ts}$ .

We plot in Fig. 6(b) the reflectivity change  $\delta R$  measured when a single *Allium cepa* cell is placed on the top surface of the transducer. In this case we observe Brillouin oscillations at a frequency of  $5.6 \pm 0.1$  GHz in the vacuole. Using the refractive index of the cell  $n_v = 1.35$  [47], we obtain the sound velocity in the cell

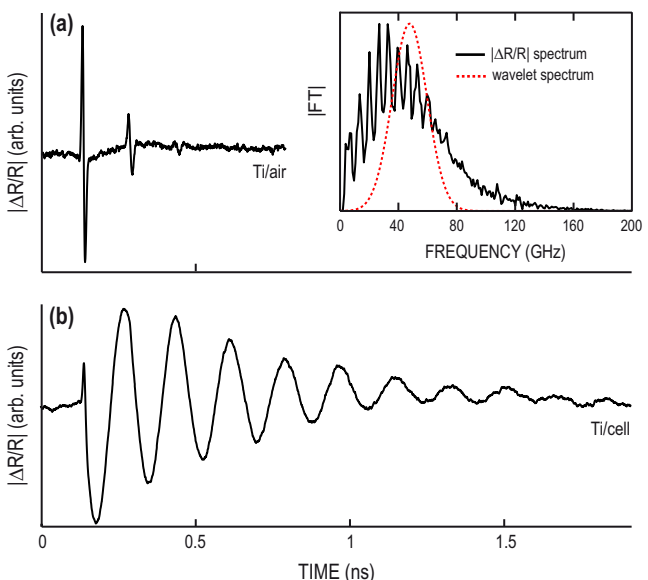


**Fig. 6.** (a) Optical reflectivity variation  $\delta R$  measured for the bare Ti-SiO<sub>2</sub> transducer. Inset: Fourier spectra of the acoustic echoes in bare Ti (black) and of the wavelet (red dotted line). (b) Optical reflectivity variation for a single cell on the Ti-SiO<sub>2</sub> transducer. (For interpretation of the references to color in this figure legend, the reader is referred to the web version of this article.)

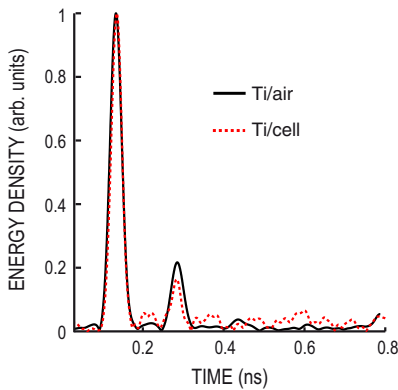


**Fig. 7.** Convolution of  $\delta R$  with a single Morlet wavelet of center frequency 50 GHz for bare Ti (plain) and Ti-cell (dashed).

$v_v = 1660 \pm m s^{-1}$  from Eq. (1), the expected value for such a cell, as seen in the previous section. The acoustic echoes are hidden by the high-amplitude Brillouin oscillations and are not visible to the naked eye. The convolution plotted in Fig. 7 with a dotted line reveals the first two echoes. These results are normalized to the amplitude of the first echo in order to observe the reflection coefficient. We observe that the second echo is smaller when a cell is placed on the transducer owing to partial transmission to the cell. The ratio of the second echo measured in the case of Ti-cell to the second echo measured in Ti yields the acoustic reflection coefficient  $R_{tc} = 0.77 \pm 0.01$  at the Ti-cell interface.<sup>4</sup> Using the value of  $Z_t$  found previously, we obtain the acoustic impedance of the cell  $Z_v = 2.6 \pm 0.1 \text{ MPa s m}^{-1}$ . Using the sound velocity in the cell  $v_v = 1660 \text{ m s}^{-1}$  obtained from the Brillouin oscillations, we convert this value into a density  $\rho_v = 1550 \pm 200 \text{ kg m}^{-3}$  for the cell. The compressibility is thus  $\chi_v = 1/\rho_v v_v = 1.0 \pm 0.1 \text{ GPa}^{-1}$ . Although the literature is very scarce, one would expect a density close to  $\sim 1100 \text{ kg m}^{-3}$  given that the vacuole is essentially composed of water [79]. Let us explain the reason for our finding of a higher value.

Indeed in the present analysis the velocity is assumed to remain constant over the frequency range spanning from the Brillouin frequency 5.6 GHz at which it is measured to the wavelet frequency 50 GHz at which the impedance is measured. If we now assume a constant density  $\sim 1100 \text{ kg m}^{-3}$  typically found in normally hydrated tissues [79], we find a velocity of  $v_v = Z_v/\rho_v = 2300 \text{ m s}^{-1}$  at the 50 GHz wavelet frequency. This velocity is much higher than the value of  $1660 \text{ m s}^{-1}$  measured at 5.6 GHz. Such a variation of the velocity over one decade is unlikely to be attributed solely to the viscous behavior of the vacuole since it has a low attenuation of  $\sim 1.6 \mu\text{m}^{-1}$  [22]. One should rather consider that the presence of the plasma membrane, which encloses the vacuole, forms a nanometric layer of thickness  $h \approx 3\text{--}10 \text{ nm}$  and of rigidity  $C$ , sandwiched between the transducer and the vacuole. Since  $h$  is much smaller than the probe wavelength in the cell  $\lambda_{pb}/2n_c \approx 300 \text{ nm}$ , this layer acts as a contacting spring of stiffness per unit area  $K = C/h$ . This cell compartment may therefore induce a frequency dependence of  $R_{tc}$  [80], and cause dispersion on the extracted velocity. This sensitivity to the state of the interface suggests important potentiality to probe the mechanics of cell-metal interactions.

#### 4. Animal-cell adhesion on metallic surfaces

The measurement of picosecond ultrasonic pulses reflected from contacting interfaces using the optical pump and probe

technique has been demonstrated to be a promising tool for the investigation of interfacial bonding [81–84] and for the characterization of nanoscale mechanical contacts between solids [77,85,86]. We here demonstrate the ability of this technique to perform quantitative label-free imaging of non-specific contacts of single mammalian cells with metallic substrates.

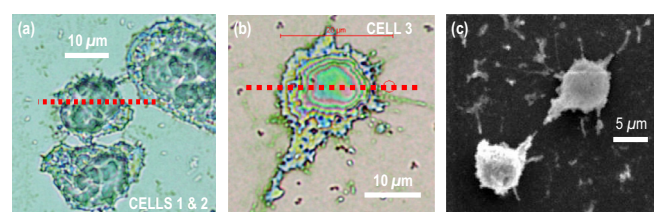
#### 4.1. Probing of the metal-cell interface using GHz acoustic waves

To study cell-metal interactions, we consider single monocytes as model animal cells. They are composed almost entirely of a nucleus and are known to display an homogeneous adhesion pattern when not migrating [87]. Their adhesion is mediated by a nanoscale meshwork of transmembrane proteins that serve as anchors for the F-actin structuration. Since their adhesion and morphology have been well characterized by fluorescent imaging, monocytes are particularly well suited to demonstrate the ability of our technique to probe cell contact. Since animal cells are more sensitive to temperature variations than vegetal cells, we use a Ti-Al<sub>2</sub>O<sub>3</sub> transducer to reduce heating at the Ti-cell interface. A polycrystalline Ti film of thickness  $d = 300 \pm 5 \text{ nm}$  with columnar structure was sputtered on a (0001) sapphire plate of thickness 1 mm by physical vapor deposition (PVD). The rms (root mean square) roughness of the Ti film surface determined by optical profilometry is 10 nm.

Monocytes were subconfluently cultured on the Ti surface and fixed with paraformaldehyde (4%) diluted in PBS for 20 min at 4 °C [88]. Mouse monocytes (RAW 264.7; ATCC, France) were cultured in alpha-MEM (Gibco) supplemented with 10% fetal calf serum (Invitrogen) and 1% penicillin/streptomycin (Invitrogen). All cells were used at low passage numbers (passage 4–8), were subconfluently cultured and plated at 10<sup>4</sup> cells/cm<sup>2</sup>. PBS was removed prior to ultrasonic investigation. Fig. 8(a) and (b) shows top-view white-light images of the probed areas, and Fig. 8(c) shows scanning electron microscope image of monocytes cultured on Ti6Al4V.

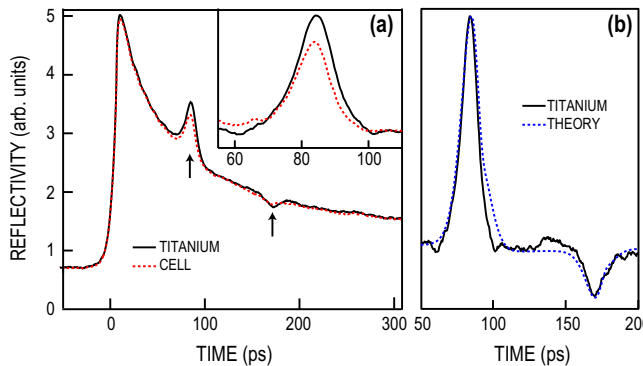
The coaxial pump (800 nm) and probe (400 nm) beams were both focused through Al<sub>2</sub>O<sub>3</sub> at the Ti-Al<sub>2</sub>O<sub>3</sub> interface with a 50× objective lens (NA 0.8) to spots of radii  $\sim 1.6$  and  $\sim 0.8 \mu\text{m}$  (intensity at 1/e<sup>2</sup>), respectively (see Fig. 2). In this configuration, no laser light reaches the Ti-cell interface, making this approach completely non-invasive [24]. The probe spot radius defines the lateral resolution. The sample was laterally scanned using a high precision translation stage so that the laser spots travel along a line with step 1 μm at the Ti-Al<sub>2</sub>O<sub>3</sub> interface. The acoustic pulse propagates through the Ti layer and thereby probes remotely the opposite Ti-cell interface, also with step 1 μm [see red dotted lines in Fig. 8(a) and (b)].

Fig. 9(a) shows the optical reflectivity change  $\delta R$  in the bare Ti region  $\sim 5 \mu\text{m}$  away from the cell edge (black plain line), and at the center of the cell nucleus (red dotted line). For  $t < 0$ ,  $\delta R$  shows



**Fig. 8.** (a) and (b) White-light image of the probed areas. The scanned lines are indicated with red dotted lines. Scale bar: 10 μm. (c) Scanning electron microscope image of monocytes cultured on Ti6Al4V. Scale bar: 5 μm. (For interpretation of the references to color in this figure legend, the reader is referred to the web version of this article.)

<sup>4</sup> The estimated error on  $R_{tc}$  corresponds to the noise level observed on Fig. 6. We estimated the subsequent errors on the impedance and mass density by differentiating the equations we used to calculate them.



**Fig. 9.** (a) Optical reflectivity change probed in the bare Ti area (black plain line) and in the cell area (red dashed line). Acoustic echoes are indicated by arrows. Inset: zoom-in on the first echo, with a polynomial subtracted for clarity. (b) Zoom-in on the echoes measured (black plain line) and calculated (blue dashed line) in the bare Ti region, with a polynomial subtracted for clarity. (For interpretation of the references to color in this figure legend, the reader is referred to the web version of this article.)

an offset due to thermal waves generated at the modulation frequency  $f_m$ . At  $t = 0$  we observe a sudden rise ( $\sim 1$  ps) in  $\delta R$  due to overheated electrons generated by the laser absorption in Ti in the vicinity of the Ti-Al<sub>2</sub>O<sub>3</sub> interface. This is followed for  $t > 0$  by a slower decrease with a characteristic time of 0.1 ns owing to heat diffusion, involving frequencies greater than the laser repetition frequency  $f_r = 80$  MHz. The contributions to the reflectivity arising from overheated electrons and from thermal diffusion remain unaffected by the presence of the cell in the probed area. This demonstrates that the thermal waves of frequencies greater than 80 MHz, as well as overheated electrons, do not reach the Ti top surface. The cell is thus thermally insulated from the laser heating, as explained in the previous section.

In addition to these thermal contributions, a compressive strain pulse is generated at  $t = 0$  in the Ti film over the optical skin depth. This pulse is reflected from the Ti free surface (or Ti-cell interface) with a reflection coefficient  $r_{ac}$ . It is detected at the Ti-Al<sub>2</sub>O<sub>3</sub> interface as an echo at time  $\sim 85$  ps. Successive reflections at the film boundaries give rise to a second echo detected at time  $\sim 170$  ps. The echoes are indicated with arrows in Fig. 9(a). The time delay  $\Delta t = 85$  ps between the two echoes corresponds to a sound velocity in the Ti film of  $V_t = 2d/\Delta t \approx 7$  nm/ps. The velocity in the Ti film is higher than that reported in bulk Ti owing to the columnar structure induced by the PVD deposition. Using the impedance of Al<sub>2</sub>O<sub>3</sub>,  $Z_s = 44$  MPa s m<sup>-1</sup> [89], we calculated the propagation of the longitudinal strain pulse  $\eta(x, t)$  in the Ti film by solving the elastic wave equation [24]. This strain modulates the dielectric permittivity of Ti of a quantity  $\delta\epsilon(x, t) \propto \eta(x, t)$  through photoelastic coupling. The ensuing theoretical optical reflectivity change was obtained from Maxwell's equation [30]. Predictions for the bare Ti region are plotted in Fig. 9(b). Considering the density 4.5 g m<sup>-3</sup> of bulk Ti gave the best fit to the data. From this value and  $V_t$  we obtained the acoustic impedance of the Ti film,  $Z_t = 32$  MPa s m<sup>-1</sup>. This approach describes precisely the acoustic reflection at the Ti free surface.

To scrutinize the variation of the echo amplitude across the cell as a function of the acoustic frequency, we convolved  $\delta R(t)$  with the Morlet wavelet  $W_m$ . The so-obtained position-frequency map shows a frequency dependence of the acoustic amplitude that is correlated to the presence of the cell in the probed area, as demonstrated in the following. This map also contains a frequency dependence of the acoustic amplitude that does not vary with position, owing to the frequency spectrum of the thermoelastic source located at the Ti-Al<sub>2</sub>O<sub>3</sub> interface. In order to observe only the

contribution of the cell to frequency dependence, we normalized the position-frequency diagram by the spectrum of the acoustic pulse reflected in the bare Ti region. This normalization yields the acoustic reflection coefficient  $r_{ac}$ . A plot of  $r_{ac}$  vs position is shown in Fig. 10(a) and (b) in 1 μm steps for frequencies 30 and 60 GHz (black and gray lines, respectively).

In Fig. 10(a) [resp. Fig. 10(b)], bare Ti regions are observed at points 1–4 μm and 23–27 μm [resp. points 1–4 μm and 28–32 μm], where  $r_{ac} > 0.9$  and is largely constant with frequency. Conversely, in Fig. 10(a) [resp. Fig. 10(b)] the presence of the cells produces a decrease of  $r_{ac}$  between  $\sim 5$  and  $\sim 22$  μm and beyond  $\sim 27$  μm [resp. between  $\sim 5$  and  $\sim 27$  μm] owing to acoustic transmission to the cells. The magnitude of the decrease of  $r_{ac}$  depends strongly on the acoustic frequency, and this effect is particularly visible around 20 μm in Fig. 10(a). The variation of  $r_{ac}$  with frequency obtained with the wavelet analysis is plotted in Fig. 11(a) at three points in the first cell [at 8, 14 and 21 μm in Fig. 10(a)]. These positions are indicated with red dots in Fig. 10(a). To elucidate the observed frequency-dependent behavior, let us consider a simple contact theory.

#### 4.2. Acoustic dispersion reveals local contact stiffness and cell acoustic impedance

Upon impinging on the contacting interface, the strain pulse induces a stress  $\sigma$  and changes the separation distance  $\Delta u$  between the cell and the biomaterial by less than 1 pm at our frequencies. To relate  $\sigma$  and  $\Delta u$ , we introduced a position-dependent massless spring of stiffness per unit area  $K = -\sigma/\Delta u$  [90]. For tightly bonded interfaces, a large stress is required to induce a small separation distance and  $K \rightarrow +\infty$ . Conversely,  $K \rightarrow 0$  for a weak bonding. Using this formalism, the acoustic reflection coefficient predicted from the acoustic wave equation is then [91]:

$$r_{ac} = \frac{|Z_t - Z_c + i\omega Z_t Z_c / K|}{|Z_t + Z_c + i\omega Z_t Z_c / K|} \quad (8)$$

where  $Z_c$  and  $\omega$  are the acoustic impedance of the cell and the angular frequency, respectively. This formula shows that the variation of  $r_{ac}$  across the cell can be attributed to changes in the cell impedance, owing to rigidity and density fluctuations within the cell. It also demonstrates that a weak Ti-cell contact would result in an increase in  $r_{ac}$  with increasing frequency, from the reflection coefficient for a perfect interface  $r_{ac} = (Z_t - Z_c)/(Z_t + Z_c)$  at low frequencies to that of a free surface  $r_{ac} = 1$  at high frequencies, as observed in Fig. 10(b).

Using the value of  $Z_t$  previously determined, we fitted Eq. (8) to the measured  $r_{ac}$  vs  $\omega$  by adjusting only  $Z_c$  and  $K$  with a least mean

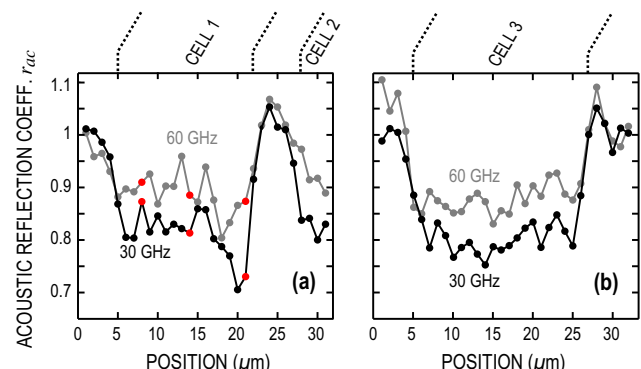


**Fig. 10.** (a) and (b) Acoustic reflection coefficient  $r_{ac}$  across the cell contact area at frequencies 30 GHz (black) and 60 GHz (gray) for cells shown in Fig. 8(a) and (b), respectively.

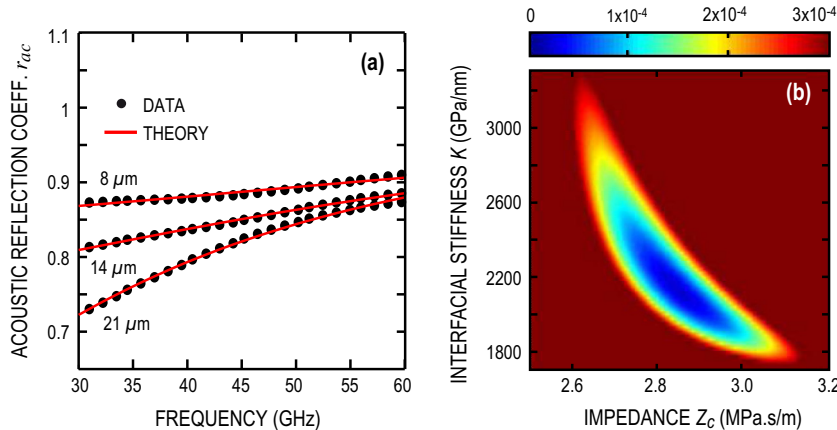


**Fig. 11.** (a) Measured (black plain line) and theoretical (red dashed line)  $r_{ac}$  vs frequency at three positions in the first cell (8, 14 and 20  $\mu\text{m}$ ). These positions are indicated in Fig. 10(a) with red dots. (b) Sum of squared errors calculated after processing a signal measured at a typical point in the in-contact region as a function of the free parameters  $K$  and  $Z_c$ . (For interpretation of the references to color in this figure legend, the reader is referred to the web version of this article.)

square procedure for each position probed in the cell region. For each point, we recorded the acoustic reflection coefficient  $r_{ac}(\omega_i)$ , where  $\omega_i$  is the discretized angular frequency. To this data we fitted  $r'_{ac}$  estimated from Eq. (2) using  $K$  and  $Z_c$  as free parameters in a least-mean-square procedure. We calculated the sum of squared errors as  $\text{sse} = \sum_i [r_{ac}(\omega_i) - r'_{ac}(\omega_i)]^2$ . We plot sse obtained at a typical point in the in-contact region in Fig. 11(b). Firstly we see that there is only one local minimum. Secondly, we see that this minimum shows a clear dip: we can therefore determine the impedance  $Z_c$  and interfacial stiffness  $K$  separately. Considering  $\text{sse} \leq 1 \times 10^{-4}$ ,  $1800 < K < 2600$  GPa/nm and  $2.7 < Z_c < 3$  MPa.s/m. Using this criterion, we get an uncertainty of 15% for  $K$  and 5% for  $Z_c$  as estimated by our procedure. Clearly we are more sensitive to variations in  $Z_c$ , leading to a better estimation.

We plot typical fits with red dashed lines in Fig. 11(a) for points 8, 14 and 21  $\mu\text{m}$  [indicated by red dots in Fig. 10(a)]. This procedure allows converting the frequency-dependent  $r_{ac}$  into separate measurements of  $Z_c$  and  $K$ . We plot  $Z_c$  and  $K$  obtained from  $r_{ac}$  shown in Fig. 10(a) [resp. Fig. 10(b)] in Fig. 12(a) and (b) [resp. Fig. 13(a) and (b)] as a function of position, respectively. For measurement points located in the Ti/air region, there is no frequency dependence. Equation (8) obviously does not apply since there is no cell in contact. In this case, we set the impedance to zero for comparison. We observe in Fig. 10(a) a strong frequency dependence at point 28  $\mu\text{m}$  on the edge of the second cell, with  $r_{ac}$  close to 1 at 60 GHz. This leads to an anomalously high cell impedance. Indeed at the cell edge the cell thickness can be of a few tens of nanometers, comparable to the acoustic wavelength. This can trigger an acoustic resonance of the cell, and cause a heightened frequency dispersion [37].

Since monocytes are composed almost entirely of a nucleus [87], we assume that the cell impedance at the center of the monocyte is that of the nucleus. We have simultaneously measured the sound velocity  $V_c \approx 3700 \text{ m s}^{-1}$  from Brillouin scattering at 25 GHz in the nucleus of monocytes, in an experimental configuration similarly to that described in Section 2. Excepting points at 20, 21 and 28  $\mu\text{m}$  in Fig. 10(a) which show a higher impedance value,  $Z_c$  is largely constant with position and defines the nominal nucleus impedance  $Z_c = 4.6 \text{ MPa s/m}$ . The nominal nucleus density is thus  $\rho_c = Z_c/V_c \approx 1250 \text{ kg m}^{-3}$ . This value is higher than that of water, as expected in the crowded nuclear space [92]. The stiffness  $K$  at the Ti-cell interface has an average value of  $\sim 1.7 \text{ GPa/nm}$ .<sup>5</sup> As a

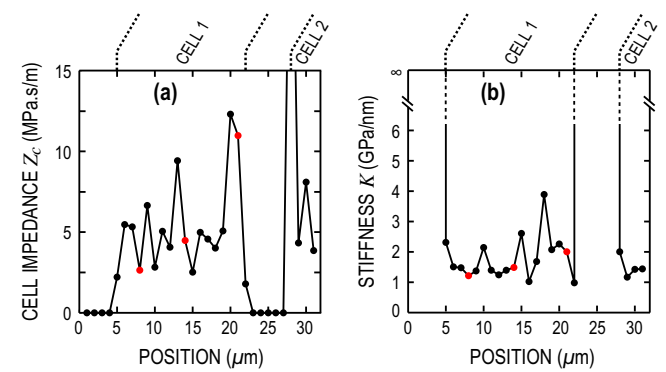


**Fig. 12.** (a) Acoustic impedance and (b) interfacial stiffness per unit area across the cell contact area obtained from  $r_{ac}$  shown in Fig. 10(a). Red dots indicate the typical points plotted in Fig. 10(a). (For interpretation of the references to color in this figure legend, the reader is referred to the web version of this article.)

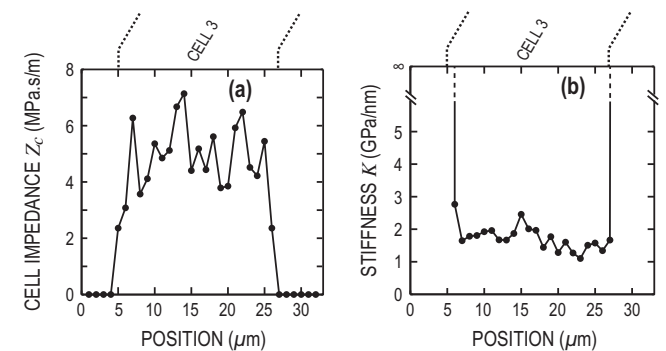


**Fig. 13.** (a) Acoustic impedance and (b) interfacial stiffness per unit area across the cell contact area obtained from  $r_{ac}$  shown in Fig. 10(b).

comparison, this is eight times smaller than the interfacial stiffness measured at similar frequencies at a gold–silicon interface [81], and three times smaller than that of octadecanethiolate molecules [93]. This points to a weak contact force of cells on Ti.

The largely homogeneous impedance and interfacial stiffness patterns are consistent with the flat fluorescence intensity profiles observed for non-migrating monocytes [87]. However, our technique also shows a larger interfacial stiffness at 10, 15 and 18  $\mu\text{m}$ , revealing an up to twofold increased adhesion. In addition,

<sup>5</sup> For illustration, the absence of cell is symbolized by an infinite value representing a perfect contact.

in a particular area located near the righthand-side edge of the first cell (around  $\sim 20 \mu\text{m}$ ) we observe in Fig. 10(a) an enhanced acoustic transmission. Observation of Fig. 12 reveals that it mostly corresponds to an increase in  $Z_c$ . This suggest an increase in the cell density and a cell stiffening owing to F-actin structural reorganization at the cell edge [87]. Such phenomenon can occur if the stability of the cell is disrupted, like in the case of migration, or if a laminar flow is applied.

To relate  $Z_c$  and  $K$  to biological quantities, it is necessary to evaluate the acoustic wavelength inside the cell. The sound velocity in the nucleus of monocytes  $V_c \approx 3700 \text{ m s}^{-1}$  yields an acoustic wavelength  $\lambda_{ac} \sim 100 \text{ nm}$  at our probed frequencies. The interfacial stiffness  $K$  is often viewed as a layer of longitudinal rigidity  $E$  and thickness  $h$  such that  $K = E/h$  at wavelengths  $\lambda_{ac} \gg h$  [94]. Any structure much smaller than  $\lambda_{ac}$  close to the interface will modify  $K$ , whereas larger structures will modify  $Z_c$ . The stiffness per unit area  $K$  we measured thus describes the interfacial intermolecular forces and also includes the contribution of cell components located in the vicinity of the cell-Ti interface that are much thinner than  $\lambda_{ac} \sim 100 \text{ nm}$ .

## 5. Conclusions

We presented a new optoacoustic-based approach for probing the mechanical properties of single cells. The small amplitude of the applied acoustic deformation, together with the remote laser generation and detection, makes this method inherently and completely non-invasive. Contrary to contact-based techniques like AFM, micropipette aspiration or bead cytometry, PU offers a unique means by which to investigate the intrinsic mechanical properties of sub-cell components. A lateral resolution of  $1 \mu\text{m}$ , and a depth resolution better than  $100 \text{ nm}$  can be achieved with this technique. We have established onion cells as a simple, widely available and well documented biological model to develop application of PU to single cell biology. To mimic the polymer-like rheological behavior of animal cells at GHz frequencies, we have also developed a confined polymer system based on microcapsules.

In view of obtaining more information on the mechanical properties of cells, we have designed and characterized an opto-acoustic transducer for biological purposes. The configuration where the probe is focused on the top surface of the transducer allows simultaneous determination of the density and of the compressibility of single cells. This should prove invaluable to understand the variation of the mechanical properties of cells under various physiological conditions, such as changes in pH or calcium concentration. These results obtained on vegetal cells also indicated that the presence of the plasma membrane enclosing the vacuole may induce a frequency dependence of the reflection coefficient.

We have used this high sensitivity to the state of the interface to probe the mechanics of cell-metal interactions. The time-frequency analysis of the reflected acoustic pulses gave access to a map of the cell acoustic impedance  $Z_c$  and to a map of the film-cell interfacial stiffness  $K$  simultaneously. Variations in  $Z_c$  across the cell are attributed to rigidity and density fluctuations within the cell, whereas variations in  $K$  are related to interfacial intermolecular forces and to the nano-architecture of the transmembrane bonds. This innovative approach allows investigating quantitatively cell-biomaterial interactions without fluorescent labels or mechanical contact to the cell.

Picosecond ultrasonics is a mature technique for probing solids. Its challenging application to soft matter is now expanding rapidly, with numerous applications. In particular, studies are under way to measure the shear modulus of cells using shear acoustic waves or interfacial waves, thereby complementing the information obtained by analyzing the longitudinal modulus. The innovative

detection of laser-generated acoustic waves will permit the exploration of a wide frequency range, shedding new light on the rheological and adhesive behavior of cells. Subsequent integration of this technique with state-of-the-art cell micromanipulation tools and imaging platforms will open new areas for the investigation of physiological processes at a sub-cell scale.

## Acknowledgements

We acknowledge financial support from the Agence Nationale de la Recherche (Grants Nos. ANR-07-BLAN-0303 and ANR-13-BS09-0021-01), the Region Aquitaine, the competitiveness cluster “Route des Lasers” and the GIS Advanced Materials in Aquitaine.

## References

- [1] N. Wang, J.D. Tytell, D.E. Ingber, Mechanotransduction at a distance: mechanically coupling the extracellular matrix with the nucleus, *Nat. Rev. Mol. Cell Biol.* 10 (1) (2009) 75–82, <http://dx.doi.org/10.1038/nrm2594>.
- [2] A.J. Engler, S. Sen, H.L. Sweeney, D.E. Discher, Matrix elasticity directs stem cell lineage specification, *Cell* 126 (2006) 677–689, <http://dx.doi.org/10.1016/j.cell.2006.06.044>.
- [3] A. Buxboim, I.L. Ivanovska, D.E. Discher, Matrix elasticity, cytoskeletal forces and physics of the nucleus: how deeply do cells ‘feel’ outside and in?, *J. Cell Sci.* 123 (3) (2010) 297–308, <http://dx.doi.org/10.1242/jcs.041186>. arXiv:<http://jcs.biologists.org/content/123/3/297.full.pdf+html>.
- [4] N. Huebsch, P.R. Arany, A.S. Mao, D. Shvartsman, O.A. Ali, S.A. Bencherif, J. Rivera-Feliciano, D.J. Mooney, Harnessing traction-mediated manipulation of the cell/matrix interface to control stem-cell fate, *Nat. Mater.* 9 (6) (2010) 518–526, <http://dx.doi.org/10.1038/nmat2732>.
- [5] Y. Sunada, S.M. Bernier, A. Utani, Y. Yamada, K.P. Campbell, Identification of a novel mutant transcript of laminin alpha 2 chain gene responsible for muscular dystrophy and dysmyelination in dy2j mice., *Hum. Mol. Genet.* 4 (6) (1995) 1055–1061.
- [6] T. Sullivan, D. Escalante-Alcalde, H. Bhatt, M. Anver, N. Bhat, K. Nagashima, C.L. Stewart, B. Burke, Loss of a-type lamin expression compromises nuclear envelope integrity leading to muscular dystrophy, *J. Cell Biol.* 147 (5) (1999) 913–920.
- [7] M.L. Lombardi, J. Lammerding, Altered mechanical properties of the nucleus in disease, in: G. Shivashankar (Ed.), *Nuclear Mechanics & Genome Regulation, Methods in Cell Biology*, vol. 98, Academic Press, 2010, pp. 121–141, [http://dx.doi.org/10.1016/S0091-679X\(10\)98006-0](http://dx.doi.org/10.1016/S0091-679X(10)98006-0) (Chapter 6).
- [8] M. Crisp, Q. Liu, K. Roux, J. Rattner, C. Shanahan, B. Burke, P.D. Stahl, D. Hodzic, Coupling of the nucleus and cytoplasm: role of the LINC complex, *J. Cell Biol.* 172 (1) (2006) 41–53, <http://dx.doi.org/10.1083/jcb.200509124>. arXiv:<http://jcb.rupress.org/content/172/1/41.full.pdf+html>.
- [9] F. Chowdhury, S. Na, D. Li, Y.-C. Poh, T.S. Tanaka, F. Wang, N. Wang, Material properties of the cell dictate stress-induced spreading and differentiation in embryonic stem cells, *Nat. Mater.* 9 (1) (2010) 82–88, <http://dx.doi.org/10.1038/nmat2563>.
- [10] J.S. Burmeister, L.A. Olivier, W. Reichert, G.A. Truskey, Application of total internal reflection fluorescence microscopy to study cell adhesion to biomaterials, *Biomaterials* 19 (4–5) (1998) 307–325, [http://dx.doi.org/10.1016/S0142-9612\(97\)00109-9](http://dx.doi.org/10.1016/S0142-9612(97)00109-9).
- [11] Y. Iwanaga, D. Braun, P. Fromherz, No correlation of focal contacts and close adhesion by comparing GFP-vinculin and fluorescence interference of Dil, *Eur. Biophys. J.* 30 (1) (2001) 17–26, <http://dx.doi.org/10.1007/s002490000119>.
- [12] M. Holt, Y. Calle, D. Sutton, D. Critchley, G. Jones, G. Dunn, Quantifying cell-matrix adhesion dynamics in living cells using interference reflection microscopy, *J. Microsc.* 232 (1) (2008) 73–81, <http://dx.doi.org/10.1111/j.1365-2818.2008.02069.x>.
- [13] W. Wang, S. Wang, Q. Liu, J. Wu, N. Tao, Mapping single-cell-substrate interactions by surface plasmon resonance microscopy, *Langmuir* 28 (37) (2012) 13373–13379, <http://dx.doi.org/10.1021/la301712h>. arXiv:<http://pubs.acs.org/doi/pdf/10.1021/la301712h>.
- [14] G. Sagvolden, I. Giaever, E. Petersen, J. Feder, Cell adhesion force microscopy, *Proc. Nat. Acad. Sci.* 96 (2) (1999) 471–476.
- [15] A. Simon, M.-C. Durrieu, Strategies and results of atomic force microscopy in the study of cellular adhesion, *Micron* 37 (1) (2006) 1–13, <http://dx.doi.org/10.1016/j.micron.2005.06.006>.
- [16] A. Raman, S. Trigueros, A. Cartagena, A.P.Z. Stevenson, M. Susilo, E. Nauman, S.A. Contera, Mapping nanomechanical properties of live cells using multi-harmonic atomic force microscopy, *Nat. Nanotechnol.* 6 (12) (2011) 809–814, <http://dx.doi.org/10.1038/nano.2011.186>.
- [17] Z. Li, J. Song, G. Martini, M.-Y. Lu, H. Fang, C. Falconi, L.-J. Chen, Z.L. Wang, Quantifying the traction force of a single cell by aligned silicon nanowire array, *Nano Lett.* 9 (10) (2009) 3575–3580, <http://dx.doi.org/10.1021/nl901774m>.
- [18] I. Schoen, W. Hu, E. Klotzsch, V. Vogel, Probing cellular traction forces by micropillar arrays: contribution of substrate warping to pillar deflection, *Nano Lett.* 10 (5) (2010) 1823–1830, <http://dx.doi.org/10.1021/nl100533c>.

- [19] Y. Zhao, C.C. Lim, D.B. Sawyer, R. Liao, X. Zhang, Microchip for subcellular mechanics study in living cells, *Sens. Actuators B* 114 (2) (2006) 1108–1115, <http://dx.doi.org/10.1016/j.snb.2005.07.071>.
- [20] Y. Tseng, J.S.H. Lee, T.P. Kole, I. Jiang, D. Wirtz, Micro-organization and viscoelasticity of the interphase nucleus revealed by particle nanotracking, *J. Cell Sci.* 117 (10) (2004) 2159–2167, <http://dx.doi.org/10.1242/jcs.01073>.
- [21] B.D. Hoffman, G. Massiera, K.M. Van Citters, J.C. Crocker, The consensus mechanics of cultured mammalian cells, *Proc. Natl. Acad. Sci.* 103 (27) (2006) 10259–10264, <http://dx.doi.org/10.1073/pnas.0510348103>. arXiv:<http://www.pnas.org/content/103/27/10259.full.pdf+html>.
- [22] C. Rossignol, N. Chigarev, M. Ducouso, B. Audoin, G. Forget, F. Guillemot, M.C. Durrieu, In Vitro picosecond ultrasonics in a single cell, *Appl. Phys. Lett.* 93 (12) (2008) 123901, <http://dx.doi.org/10.1063/1.2988470>.
- [23] B. Audoin, C. Rossignol, N. Chigarev, M. Ducouso, G. Forget, F. Guillemot, M.C. Durrieu, Picosecond acoustics in vegetal cells: non-invasive in vitro measurements at a sub-cell scale, *Ultrasonics* 50 (2) (2010) 202–207, <http://dx.doi.org/10.1016/j.ultras.2009.09.019>.
- [24] T. Dehoux, B. Audoin, Non-invasive optoacoustic probing of the density and stiffness of single biological cells, *J. Appl. Phys.* 112 (12) (2012) 124702, <http://dx.doi.org/10.1063/1.4769294>.
- [25] A. Gadalla, T. Dehoux, B. Audoin, Transverse mechanical properties of cell walls of single living plant cells probed by laser-generated acoustic waves, *Planta* 239 (5) (2014) 1129–1137, <http://dx.doi.org/10.1007/s00425-014-2045-y>.
- [26] M. Abi Ghanem, T. Dehoux, O.F. Zouani, A. Gadalla, M.-C. Durrieu, B. Audoin, Remote opto-acoustic probing of single-cell adhesion on metallic surfaces, *J. Biophotonics* 7 (6) (2014) 453–459, <http://dx.doi.org/10.1002/jbio.201300098>.
- [27] M. Ducouso, O. El-Farouk Zouani, C. Chanseau, C. Chollet, C. Rossignol, B. Audoin, M.-C. Durrieu, Evaluation of mechanical properties of fixed bone cells with sub-micrometer thickness by picosecond ultrasonics, *Eur. Phys. J. – Appl. Phys.* 61 (2013) 11201, <http://dx.doi.org/10.1051/epjap/2012120279>.
- [28] T. Dehoux, N. Tsapis, B. Audoin, Relaxation dynamics in single polymer microcapsules probed with laser-generated GHz acoustic waves, *Soft Matter* 8 (2012) 2586–2589, <http://dx.doi.org/10.1039/C2SM07146K>.
- [29] C. Thomsen, J. Strait, Z. Vardeny, H.J. Maris, J. Tauc, J.J. Hauser, Coherent phonon generation and detection by picosecond light pulses, *Phys. Rev. Lett.* 53 (10) (1984) 989–992, <http://dx.doi.org/10.1103/PhysRevLett.53.989>.
- [30] C. Thomsen, H.T. Grahn, H.J. Maris, J. Tauc, Surface generation and detection of phonons by picosecond light pulses, *Phys. Rev. B* 34 (6) (1986) 4129–4138.
- [31] O. Wright, V. Gusev, Ultrafast generation of acoustic waves in copper, *IEEE Trans. Ultrason. Ferroelectr. Freq. Control* 42 (3) (1995) 331–338.
- [32] O.B. Wright, B. Perrin, O. Matsuda, V.E. Gusev, Ultrafast carrier diffusion in gallium arsenide probed with picosecond acoustic pulses, *Phys. Rev. B* 64 (8) (2001) 081202.
- [33] A. Devos, M. Foret, S. Ayrimac, P. Emery, B. Ruffié, Hypersound damping in vitreous silica measured by picosecond acoustics, *Phys. Rev. B* 77 (10) (2008) 100201, <http://dx.doi.org/10.1103/PhysRevB.77.100201>.
- [34] H.J. Maris, Picosecond ultrasonics, *Sci. Am.* 278 (1998) 64–67.
- [35] G. Tas, H. Maris, Picosecond ultrasonic study of phonon reflection from solid-liquid interfaces, *Phys. Rev. B* 55 (3) (1997) 1852–1857.
- [36] F. Yang, T.J. Grimsley, S. Che, G.A. Antonelli, H.J. Maris, A.V. Nurmikko, Picosecond ultrasonic experiments with water and its application to the measurement of nanostructures, *J. Appl. Phys.* 107 (10) (2010) 103537, <http://dx.doi.org/10.1063/1.3388283>.
- [37] L. Rouai, B. Bonello, G. Louis, B. Perrin, P. Peretti, Elasticity of ultrathin copper-phthalocyanine Langmuir–Blodgett films by picosecond ultrasonics, *J. Appl. Phys.* 85 (12) (1999) 8155–8159.
- [38] A. Devos, B. Perrin, B. Bonello, J.-C. Jeannet, Ultra-fast photoacoustics in colloids, *AIP Conf. Proc.* 463 (1) (1999) 445–447, <http://dx.doi.org/10.1063/1.58210>.
- [39] B. Perrin, C. Rossignol, B. Bonello, J. Jeannet, Interferometric detection in picosecond ultrasonics, *Appl. Surf. Sci.* 263 (1999) 571–573, [http://dx.doi.org/10.1016/S0921-4526\(98\)01479-3](http://dx.doi.org/10.1016/S0921-4526(98)01479-3).
- [40] L. Shelton, F. Yang, W. Ford, H. Maris, Picosecond ultrasonic measurement of the velocity of phonons in water, *Phys. Status Solidi B* 242 (7) (2005) 1379–1382, <http://dx.doi.org/10.1002/pssb.200440030>.
- [41] T. Pezeril, C. Klieber, S. Andrieu, K.A. Nelson, Optical generation of GHz-frequency shear acoustic waves in liquid glycerol, *Phys. Rev. Lett.* 102 (10) (2009) 107402, <http://dx.doi.org/10.1103/PhysRevLett.102.107402>.
- [42] O.B. Wright, B. Perrin, O. Matsuda, V.E. Gusev, Optical excitation and detection of picosecond acoustic pulses in liquid mercury, *Phys. Rev. B* 78 (2) (2008) 024303, <http://dx.doi.org/10.1103/PhysRevB.78.024303>.
- [43] A.A. Maznev, K.J. Manke, C. Klieber, K.A. Nelson, S.H. Baek, C.B. Eom, Coherent Brillouin spectroscopy in a strongly scattering liquid by picosecond ultrasonics, *Opt. Lett.* 36 (15) (2011) 2925–2927, <http://dx.doi.org/10.1364/OL.36.002925>.
- [44] D. Pantaloni, C.L. Clainche, M.-F. Carlier, Mechanism of actin-based motility, *Science* 292 (5521) (2001) 1502–1506, <http://dx.doi.org/10.1126/science.1059975>. arXiv:<http://www.scienmag.org/content/292/5521/1502.full.pdf>.
- [45] K.N. Dahl, A.J. Engler, J.D. Pajerowski, D.E. Discher, Power-law rheology of isolated nuclei with deformation mapping of nuclear substructures, *Biophys. J.* 89 (4) (2005) 2855–2864.
- [46] Z. Lin, L.V. Zhigilev, V. Celli, Electron–phonon coupling and electron heat capacity of metals under conditions of strong electron–phonon nonequilibrium, *Phys. Rev. B* 77 (7) (2008) 075133, <http://dx.doi.org/10.1103/PhysRevB.77.075133>.
- [47] D. Liu, B. Kuhlmeier, P. Smith, D. Day, C. Faulkner, R. Overall, Reflection across plant cell boundaries in confocal laser scanning microscopy, *J. Microsc.* 231 (2) (2008) 349–357, <http://dx.doi.org/10.1111/j.1365-2818.2008.02068.x>.
- [48] V.A. Del Gross, C.W. Mader, Speed of sound in pure water, *J. Acoust. Soc. Am.* 52 (5B) (1972) 1442–1446, <http://dx.doi.org/10.1121/1.1913258>.
- [49] H.W. Gausman, W.A. Allen, D.E. Escobar, Refractive index of plant cell walls, *Appl. Opt.* 13 (1) (1974) 109–111, <http://dx.doi.org/10.1364/AO.13.000109>.
- [50] J.T. Woolley, Refractive index of soybean leaf cell walls, *Plant Physiol.* 55 (2) (1975), <http://dx.doi.org/10.1104/pp.55.2.172>.
- [51] D. Debavelaere-Callens, L. Peyre, P. Campistron, H.F. Hildebrand, On the use of ultrasounds to quantify the longitudinal threshold force to detach osteoblastic cells from a conditioned glass substrate, *Biomol. Eng.* 24 (5) (2007) 521–525, <http://dx.doi.org/10.1016/j.bioeng.2007.08.016>.
- [52] International Electrotechnical Commission, International Standard, Safety of Laser Products – Part 1: Equipment Classification and Requirements, IEC 60825-1. ISBN 2-8318-9085-3.
- [53] American National Standards Institute, American National Standard for the Safe Use of Lasers in Health Care Facilities: Standard Z136.1, ANSI Inc., New York, 2000.
- [54] D.W. Piston, M.S. Kirby, H. Cheng, W.J. Lederer, W.W. Webb, Two-photon-excitation fluorescence imaging of three-dimensional calcium-ion activity, *Appl. Opt.* 33 (4) (1994) 662–669, <http://dx.doi.org/10.1364/AO.33.000662>.
- [55] E. Berry, G.C. Walker, A.J. Fitzgerald, N.N. Zinov'ev, M. Chamberlain, S.W. Smye, R.E. Miles, M.A. Smith, Do in vivo terahertz imaging systems comply with safety guidelines?, *J. Laser Appl.* 15 (3) (2003) 192–198, <http://dx.doi.org/10.2351/1.1585079>.
- [56] W. Denk, J. Strickler, W. Webb, Two-photon laser scanning fluorescence microscopy, *Science* 248 (4951) (1990) 73–76.
- [57] K. König, P.T.C. So, W.W. Mantulin, E. Gratton, Cellular response to near-infrared femtosecond laser pulses in two-photon microscopes, *Opt. Lett.* 22 (2) (1997) 135–136, <http://dx.doi.org/10.1364/OL.22.000135>.
- [58] C. Verdier, J. Etienne, A. Duperray, L. Preziosi, Review: rheological properties of biological materials, *C.R. Phys.* 10 (8) (2009) 790–811, <http://dx.doi.org/10.1016/j.crhy.2009.10.003>.
- [59] B. Fabry, G.N. Maksym, J.P. Butler, M. Glogauer, D. Navajas, J.J. Fredberg, Scaling the microrheology of living cells, *Phys. Rev. Lett.* 87 (14) (2001) 148102, <http://dx.doi.org/10.1103/PhysRevLett.87.148102>.
- [60] G.B. Sukhorukov, E. Donath, S. Moya, A.S. Susha, A. Voigt, J. Hartmann, H. Möhwald, Microencapsulation by means of step-wise adsorption of polyelectrolytes, *J. Microencapsulation* 17 (2) (2000) 177–185, <http://dx.doi.org/10.1080/026520400288418>.
- [61] M. Delcea, H. Möhwald, A.G. Skirtach, Stimuli-responsive LbL capsules and nanoshells for drug delivery, *Adv. Drug Deliv. Rev.* 63 (9) (2011) 730–747, <http://dx.doi.org/10.1016/j.addr.2011.03.010>.
- [62] C. Gómez-Gaete, E. Fattal, L. Silva, M. Besnard, N. Tsapis, Dexamethasone acetate encapsulation into trojan particles, *J. Control. Release* 128 (1) (2008) 41–49, <http://dx.doi.org/10.1016/j.jconrel.2008.02.008>.
- [63] E. Pisani, N. Tsapis, B. Galaz, M. Santini, R. Bertì, N. Taulier, E. Kurtisovski, O. Lucidarme, M. Ourveich, B.T. Doan, J.C. Beloeil, B. Gillet, W. Urbach, S.L. Bridal, E. Fattal, Perfluorooctyl bromide polymeric capsules as dual contrast agents for ultrasonography and magnetic resonance imaging, *Adv. Funct. Mater.* 18 (19) (2008) 2963–2971, <http://dx.doi.org/10.1002/adfm.200800454>.
- [64] E. Pisani, N. Tsapis, J. Paris, V. Nicolas, L. Cattel, E. Fattal, Polymeric nano/microcapsules of liquid perfluorocarbons for ultrasonic imaging: physical characterization, *Langmuir* 22 (9) (2006) 4397–4402.
- [65] R. Diaz-López, N. Tsapis, D. Libong, P. Chamainade, C. Connan, M.M. Chehimi, R. Bertì, N. Taulier, W. Urbach, V. Nicolas, E. Fattal, Phospholipid decoration of microcapsules containing perfluorooctyl bromide used as ultrasound contrast agents, *Biomaterials* 30 (8) (2009) 1462–1472, <http://dx.doi.org/10.1016/j.biomaterials.2008.11.032>.
- [66] J.J. Lin, F.S. Bates, D.A. Hammer, J.A. Silas, Adhesion of polymer vesicles, *Phys. Rev. Lett.* 95 (2) (2005) 026101, <http://dx.doi.org/10.1103/PhysRevLett.95.026101>.
- [67] X. Liu, C. Gao, J. Shen, H. Möhwald, Multilayer microcapsules as anti-cancer drug delivery vehicle: deposition, sustained release, and in vitro bioactivity, *Macromol. Biosci.* 5 (12) (2005) 1209–1219, <http://dx.doi.org/10.1002/mabi.200500176>.
- [68] Y. Jing, Y. Zhu, X. Yang, J. Shen, C. Li, Ultrasound-triggered smart drug release from multifunctional coreshell capsules one-step fabricated by coaxial electrospray method, *Langmuir* 27 (3) (2011) 1175–1180, <http://dx.doi.org/10.1021/la1042734>.
- [69] H. Richardson, I. López-García, M. Sferrazza, J.L. Keddie, Thickness dependence of structural relaxation in spin-cast, glassy polymer thin films, *Phys. Rev. E* 70 (5) (2004) 051805, <http://dx.doi.org/10.1103/PhysRevE.70.051805>.
- [70] R.D. Priestley, C.J. Ellison, L.J. Broadbelt, J.M. Torkelson, Structural relaxation of polymer glasses at surfaces, interfaces, and in between, *Science* 309 (5733) (2005) 456–459, <http://dx.doi.org/10.1126/science.1112217>.
- [71] J.G. Riess, Oxygen carriers (“blood substitutes”) – raison d'être, chemistry, and some physiology, *Chem. Rev.* 101 (9) (2001) 2797–2920, <http://dx.doi.org/10.1021/cr970143c>.
- [72] J.N. Marsh, C.S. Hall, S.A. Wickline, G.M. Lanza, Temperature dependence of acoustic impedance for specific fluorocarbon liquids, *J. Acoust. Soc. Am.* 112 (6) (2002) 2858–2862, <http://dx.doi.org/10.1121/1.1517251>.

- [73] N.G. Parker, M.L. Mather, S.P. Morgan, M.J.W. Povey, Longitudinal acoustic properties of poly(lactic acid) and poly(lactic-co-glycolic acid), *Biomed. Mater.* 5 (5) (2010) 055004, <http://dx.doi.org/10.1088/1748-6041/5/5/055004>.
- [74] T.A. Litovitz, C.M. Davis, *Physical Acoustics*, vol. 2A, Academic, New York, 1965.
- [75] D. Fioretto, F. Scarponi, Dynamics of a glassy polymer studied by Brillouin light scattering, *Mater. Sci. Eng. A* 521–522 (2009) 243–246, <http://dx.doi.org/10.1016/j.msea.2008.09.095>.
- [76] T. Dehoux, B. Audoin, O. Zouani, M.C. Durrieu, Mechanical characterization of temperature-sensitive objects using picosecond ultrasonics, *J. Phys. Conf. Ser.* 278 (1) (2011) 012043, <http://dx.doi.org/10.1088/1742-6596/278/1/012043>.
- [77] T. Dehoux, O.B. Wright, R.L. Voti, V.E. Gusev, Nanoscale mechanical contacts probed with ultrashort acoustic and thermal waves, *Phys. Rev. B* 80 (23) (2009) 235409.
- [78] D.G. Cahill, Analysis of heat flow in layered structures for time-domain thermoreflectance, *Rev. Sci. Instrum.* 75 (12) (2004) 5119–5122, <http://dx.doi.org/10.1063/1.1819431>.
- [79] R. Rapusas, R. Driscoll, Thermophysical properties of fresh and dried white onion slices, *J. Food Eng.* 24 (2) (1995) 149–164, [http://dx.doi.org/10.1016/0260-8774\(94\)P2640-Q](http://dx.doi.org/10.1016/0260-8774(94)P2640-Q).
- [80] B.W. Drinkwater, R. Dwyer Joyce, P. Cawley, A study of the interaction between ultrasound and a partially contacting solid-solid interface, *Proc. Roy. Soc. London A* 452 (1955) (1996) 2613–2628.
- [81] G. Tas, J.J. Loomis, H.J. Maris, A.A. Bailes III, L.E. Seiberling, Picosecond ultrasonics study of the modification of interfacial bonding by ion implantation, *Appl. Phys. Lett.* 72 (18) (1998) 2235–2237, <http://dx.doi.org/10.1063/1.121276>.
- [82] G.A. Antonelli, B. Perrin, B.C. Daly, D.G. Cahill, Characterization of mechanical and thermal properties using ultrafast optical metrology, *MRS Bull.* 31 (8) (2006) 607–613.
- [83] M.D. Losego, M.E. Grady, N.R. Sottos, D.G. Cahill, P.V. Braun, Effects of chemical bonding on heat transport across interfaces, *Nat. Mater.* 11 (6) (2012) 502–506, <http://dx.doi.org/10.1038/nmat3303>.
- [84] M. Hettich, A. Bruchhausen, S. Riedel, T. Geldhauser, S. Verleger, D. Issenmann, O. Ristow, R. Chauhan, J. Dual, A. Erbe, E. Scheer, P. Leiderer, T. Dekorsy, Modification of vibrational damping times in thin gold films by self-assembled molecular layers, *Appl. Phys. Lett.* 98 (26) (2011) 261908, <http://dx.doi.org/10.1063/1.3604790>.
- [85] T. Dehoux, O.B. Wright, R.L. Voti, Picosecond time scale imaging of mechanical contacts, *Ultrasonics* 50 (2) (2009) 197–201, <http://dx.doi.org/10.1016/j.ultras.2009.08.008>.
- [86] T. Valier-Brasier, T. Dehoux, B. Audoin, Scaled behavior of interface waves at an imperfect solid-solid interface, *J. Appl. Phys.* 112 (2) (2012) 024904, <http://dx.doi.org/10.1063/1.4733949>.
- [87] J. Rullo, H. Becker, S.J. Hyduk, J.C. Wong, G. Digby, P.D. Arora, A.P. Cano, J. Hartwig, C.A. McCulloch, M.I. Cybulsky, Actin polymerization stabilizes 41 integrin anchors that mediate monocyte adhesion, *J. Cell Biol.* 197 (1) (2012) 115–129, <http://dx.doi.org/10.1083/jcb.201107140>. arXiv:<http://jcb.rupress.org/content/197/1/115.full.pdf+html>.
- [88] M.C. Porté-Durrieu, F. Guillemot, S. Pallu, C. Labrugère, B. Brouillaud, R. Bareille, J. Amédée, N. Barthe, M. Dard, C. Baquey, Cy clo-(dfkrg) peptide grafting onto ti-6al-4v: physical characterization and interest towards human osteoprogenitor cells adhesion, *Biomaterials* 25 (19) (2004) 4837–4846, <http://dx.doi.org/10.1016/j.biomaterials.2003.11.037>.
- [89] O.L. Anderson, Determination and some uses of isotropic elastic constants of polycrystalline aggregates using single-crystal data, in: W.P. Mason (Ed.), *Physical Acoustics*, vol. 3B, Academic, New York, 1965, pp. 43–95.
- [90] K. Kendall, D. Tabor, An ultrasonic study of the area of contact between stationary and sliding surfaces, *Proc. Roy. Soc. London A* 323 (1971) 321–340.
- [91] H.G. Tattersall, The ultrasonic pulse-echo technique as applied to adhesion testing, *J. Phys. D* 6 (1973) 819–832, <http://dx.doi.org/10.1088/0022-3727/6/7/305>.
- [92] D. Bazett-Jones, R. Li, E. Fussner, R. Nisman, H. Dehghani, Elucidating chromatin and nuclear domain architecture with electron spectroscopic imaging, *Chromosome Res.* 16 (3) (2008) 397–412, <http://dx.doi.org/10.1007/s10577-008-1237-3>.
- [93] P.-A. Mante, H.-Y. Chen, M.-H. Lin, Y.-C. Wen, S. Gwo, C.-K. Sun, Selectively probing vibrations in a plasmonic supracrystal, *Appl. Phys. Lett.* 101 (10) (2012) 101903, <http://dx.doi.org/10.1063/1.4750140>.
- [94] S.I. Rokhlin, Y.J. Wang, Analysis of boundary conditions for elastic wave interaction with an interface between two solids, *J. Acoust. Soc. Am.* 89 (2) (1991) 503–515, <http://dx.doi.org/10.1121/1.400374>.